Hussein, Abdulmenan M.; Iefanova, Anastasiia V.; Koodali, Ranjit T.; Logue, Brian A.; Shende, Rajesh V.

Article

Interconnected ZrO2 doped ZnO/TiO2 network photoanode for dye-sensitized solar cells

Energy Reports

Provided in Cooperation with:
Elsevier

Suggested Citation: Hussein, Abdulmenan M.; Iefanova, Anastasiia V.; Koodali, Ranjit T.; Logue, Brian A.; Shende, Rajesh V. (2018) : Interconnected ZrO2 doped ZnO/TiO2 network photoanode for dye-sensitized solar cells, Energy Reports, ISSN 2352-4847, Elsevier, Amsterdam, Vol. 4, pp. 56-64, https://doi.org/10.1016/j.egyr.2018.01.007

This Version is available at:
https://hdl.handle.net/10419/187903

Energy Reports 4 (2018) 56–64

Contents lists available at ScienceDirect

Energy Reports

journal homepage: www.elsevier.com/locate/egyr

Research paper

Interconnected ZrO_2 doped ZnO/TiO_2 network photoanode for dye-sensitized solar cells

Abdulmenan M. Hussein [a], Anastasiia V. Iefanova [b], Ranjit T. Koodali [c], Brian A. Logue [d], Rajesh V. Shende [e,*]

[a] Composites and Polymer Engineering Laboratory, South Dakota School of Mines and Technology, Rapid City, SD 57701, USA
[b] Meteocontrol North America, Buffalo Grove, IL, 60089, USA
[c] Department of Chemistry, University of South Dakota, Vermillion, SD 57069, USA
[d] Department of Chemistry and Biochemistry, South Dakota State University, Brookings, SD 57007, USA
[e] Department of Chemical and Biological Engineering, South Dakota School of Mines and Technology, Rapid City, SD 57701, USA

HIGHLIGHTS

- ZrO_2 surface passivated ZnO/TiO_2 photoanode is investigated for DSSC.
- ZrO_2 prevents charge recombination and improves open circuit voltage.
- Open circuit voltage is enhanced due to composite/electrolyte band edge shift.
- IPCE measurements reveal higher photons absorption and superior photocurrent.
- Longer electron life time and higher efficiency for ZrO_2 based photoanode.

GRAPHICAL ABSTRACT

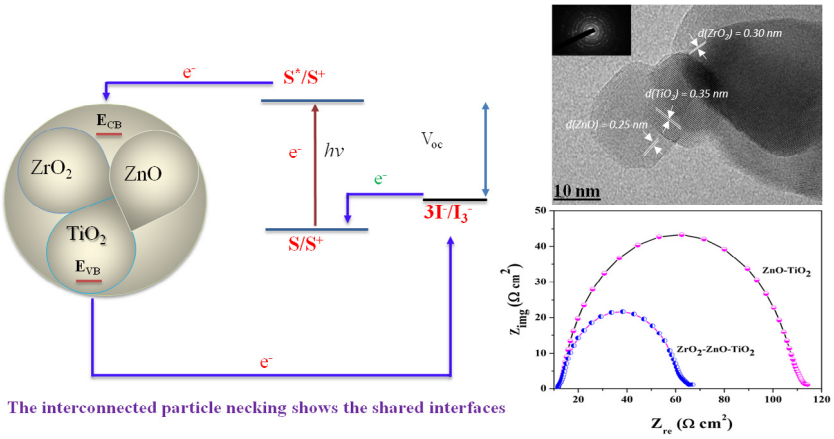

ARTICLE INFO

Article history:
Received 28 August 2017
Received in revised form 27 January 2018
Accepted 27 January 2018

Keywords:
ZrO_2 passivated ZnO/TiO_2 hetero-phase composite
Mesoporous films dye-sensitized solar cells
Dark current
Equivalent circuit model

ABSTRACT

In this study, ZrO_2 surface modified ZnO/TiO_2 composite film is adapted as photoanode in dye sensitized solar cells (DSSCs) and compared with un-passivated ZnO/TiO_2 DSSC performance. The performance is investigated by dark and photocurrent density–voltage (*J–V)* characteristics, quantum efficiency and electrochemical impedance spectroscopy. The *J–V* characteristics shows that DSSCs with ZrO_2 surface passivation produces significantly high open-circuit voltage of 0.87 V, short-circuit current density of 13.6 mA cm^{-2}, fill factor of 0.65 and a power conversion efficiency of ∼6.97% under simulated AM1.5 solar irradiation. The higher onset potential in the dark, larger open-circuit potential under illumination, and an enhancement in power conversion efficiency strongly suggests an efficient suppression of back electron transfer from the conduction band of the hetero-phase junctions to the oxidized species in the electrolyte as established by dark and illuminated *J–V* characteristics. Thus, the oxidized dye molecules are readily regenerated by a redox couple dissolved in an electrolyte, allowing more photon excitation by dye molecules. The electrochemical impedance data extracts further provide additional evidence of the enhancement in photocurrent and lower charge carrier resistances observed in ZrO_2/ZnO/TiO_2/dye

* Corresponding author.
E-mail address: rajesh.shende@sdsmt.edu (R.V. Shende).

https://doi.org/10.1016/j.egyr.2018.01.007

photoelectrode. With the ZrO_2 surface modification, main loss mechanism in the device is suppressed and backward recombination reaction is minimized.

1. Introduction

Affordable and more easily processed solar cells together with long term stable efficiency are the holy grails of renewable energy research. As such, dye sensitized solar cells (DSSCs) have attracted intense academic and technological interest because of its low fabrication cost as opposed to *p-n* junction silicon solar cells (Toivola et al., 2009). It is the only photovoltaic device that converts light energy into electrical energy using organic dyes stained metal oxide semiconductors. DSSCs have several advantages over silicon-based photovoltaics counterparts. It offers the high power conversion efficiency under low-light (i.e. cloudy skies) and artificial light conditions (Grätzel, 2005; Somasundaran et al., 2011).

In 1991, Gratzel group successfully developed DSSC based on novel electrode architecture in the form of a mesoporous TiO_2 film. The nature of the mesoporous TiO_2 network provides large specific surface area that improves dye chemisorption and light harvesting efficiency of incident photons to electrons (Grätzel, 2001; Pai et al., 2014; Docampo et al., 2014). Since the breakthrough, different TiO_2 morphologies in the form of spheres (Veerappan et al., 2014), nanowires (Lee et al., 2012), nanorods (Wang et al., 2012a) and nanotubes (Chen et al., 2009) have been widely employed in a typical device architecture. With these morphologies, different energy conversion efficiencies were observed. Through the planar nanocrystalline TiO_2 structure and ruthenium (II) based dyes, a record high power conversion efficiency of 12.3% (Yella et al., 2011) was achieved for devices prepared under high vacuum processes. Recently, high power conversion efficiency of 13% is reported by employing newly engineered porphyrin SM315 dye, (Mathew et al., 2014). However, it is still short of *p-n* junction derived solar efficiency of 25% (Green et al., 2011).

In addition to TiO_2 nanocrystals, various nanostructured metal-oxides such as ZnO (Shintaro Ueno and Fujihara, 2011), SnO_2 (Duan et al., 2015), $SrTiO_3$ (Hod et al., 2010), Fe_2O_3 (Shang et al., 2015), WO_3 (Yong et al., 2013), and binary oxides including ZnO/TiO_2 (Liu et al., 2012), ZrO_2/TiO_2 (Wang et al., 2012b), SnO_2/TiO_2 (Mohan et al., 2012), ZnO/SnO_2 (Milan et al., 2015), $SrTiO_3/TiO_2$ (Jose et al., 2009) have been actively investigated as photoelectrodes in DSSCs. In binary metal oxides, the band edge offset facilitate strong driving force for efficient charge transport and collection (Hussein et al., 2013). However, despite considerable efforts made, the overall efficiency obtained with binary system was inferior to the nanoparticle TiO_2 based films (Law et al., 2006; Chen et al., 2013).

The power conversion efficiency is the performance indicator of the DSSCs. It reflects the device ability in the light harvesting, charge separating and transferring processes. The performance largely hindered by the non-sufficient utilization of the low-energy photons (i.e. near red and near-infrared light) and difficulties in effectively extracting photo-generated electrons due to competing and spontaneous back-electron transfer reactions.

In the DSSC sandwich configuration and working mechanism, inherently complex and competitive interfacial elements exist, namely TiO_2/electrolyte, dye/electrolyte and Fluorine-doped tin oxide (FTO)/electrolyte, where physical interactions occur and carriers in separate phases meet each other. Thus, there are series of recombination reaction rates that compete with the forward reactions. The photo-generation, and subsequent charge separation and recombination occur exclusively at hetero-interfaces (Gu et al., 2017; Gao et al., 2017). The proximity of electrons and holes, and the lack of potential barrier between them lead to charge carrier's annihilation. Quite naturally, the device performance strongly depend on interfacial physical and photo–electrochemical interactions (Annamalai et al., 2011). Thus, major energy losses via recombination are almost entirely an interfacial process as opposed to bulk process in p–n junction solar cells (Gregg et al., 2001).

Energy losses associatively occur at TiO_2/electrolyte interface (Tang et al., 2013) or FTO/electrolyte interface (Ofir et al., 2008). Thermodynamically spontaneous back charge reaction between the conduction band electrons and oxidative species present in the electrolyte reduces photocurrent available to the load. Likewise, back-electron transfer reactions occur at the contact of an electrolyte with an FTO surface by a permeation mechanism, causes an electrical leakage in the device, leading to loss of the photocurrent (Smiglak et al., 2014). Specifically, dark current originates from physical contact of electrolyte with a bare conductive FTO surface due to the porous nature of the TiO_2 structure (Yu et al., 2009). Minimizing the dark current at TiO_2/electrolyte interface, will improve in an open circuit potential. Therefore, retarding the spontaneous recapture of injected electrons by oxidative species at the photoanode/electrolyte interface or blocking the current leakage at FTO/electrolyte interface is critical to extract maximum power conversion.

To address these problems, numerous approaches have been proposed to minimize the recombination losses at the interfaces. Particularly, device architectures that include metal oxide overcoats to create barrier layers with more negative conduction band potential (Palomares et al., 2003) and organic framework as additives to suppress potential-dependent dark current (Katz et al., 2012), thereby leading to reduction in current–voltage hysteresis, an increase in the open-circuit potential and the power conversion efficiency of the solar cell.

In this study, the arrangement of the photoanode constituting conjoined and ZrO_2 surface passivated ZnO/TiO_2 compact layer was investigated in DSSCs to address the aforementioned problems. The device performance was discussed in relation with the spatial photoinduced charge separation, blocking back electron transfer in the photoanode and bandgap off-set. Herein, we report improvements in solar energy conversion efficiency and high open circuit potential attributed to improved reduced current–voltage hysteresis, enhanced photon absorption and light-harvesting efficiency, effective charge transport and separation, and suppressed dark current by employing hetero-phase photoanode in the form of ZrO_2 surface passivated ZnO/TiO_2 compact layer. The recombination losses were greatly minimized as confirmed by impedance analysis and dark current measurements. The photocurrent density–voltage characteristics, incident photon-to-current efficiency *(IPCE)* and electrochemical impedance spectroscopy methods have been employed to understand the surface passivation effect of the photoanode and obtain evidence responsible for the improved open circuit potential, reduced recombination and DSSC performance. A comparative study of DSSCs performance based on ZnO/TiO_2 and ZrO_2 surface passivated ZnO/TiO_2 compact layer nanostructured electrodes is presented.

2. Experimental

2.1. Synthesis of ZrO_2 surface passivated ZnO/TiO_2 nanostructure

The ZrO_2 surface passivated ZnO/TiO_2 nanostructure was synthesized according to the previously reported method (Hussein

and Shende, 2014) with little modification. Briefly, 2.4 g titanium (IV) isopropoxide (75 wt.% TiO_2) and 0.25 g zinc acetate dihydrate (24.5 wt.% ZnO) were separately dissolved in 5 mL diethylene glycol methyl ether (DEGME) and 10 mL ethanol solution mixture containing 0.57 g Pluronic P123 ($EO_{20}PO_{70}EO_{20}$) as a structure-directing template. The precursor solutions were carefully stirred separately until a visually clear solution were obtained. The zinc solution was slowly added under magnetic stirring and then allowed to form a composite gel. The gel was then aged in a vacuum at 70 °C for 72 h. The obtained dry solid product was hand ground into a fine powder using a mortar and pestle and dispersed in water–isopropyl alcohol mixture. To this translucent colloidal dispersion, zirconium (IV) isopropoxide (0.5 wt.% ZrO_2) in isopropanol was added under vigorous magnetic stirring and heated slowly to 70 °C. Subsequently, few drops of deionized water were introduced to induce gelation. The ZrO_2 surface passivated gel was aged and dried in a glovebox under Argon environment for 72 h. The obtained hydrated metal oxides powder was processed differently to use them as compact or active layer as details preparation method found in Sections 2.3 and 2.4. For later use, portion of the hydrated powder was calcined at 600 °C in muffle furnace at ramping rate of 3 °C /min and kept at this temperature for 3 h. The composite was grind into very fine powder and suspended in deionized water/ethanol mixture. The dispersed colloidal suspension was high pressure filtered and washed several times with deionized water, and later dried in glovebox at 105 °C under Argon environment.

2.2. Cleaning electrodes

FTO conductive glass (Hartford Glass Co., 1.6 mm thick) was used as a substrate for the preparation of the photoanode and counter electrode. These glass substrates were washed using an ultrasonic bath, detergent water, deionized water and cleaned with acetone and ethanol. Finally, the glasses were rinsed with methanol and blow dried with an air stream prior to fabrication of compact layer photoanode.

2.3. Thin film compact layer preparation and coating

To prepare the photoanode with compact under-layer, a ZrO_2 surface passivated ZnO/TiO_2 hydrated translucent solution was spin coated on pre-cleaned circular area of approximately 0.25 cm^2 FTO-coated glass at 3000 rpm for 20 s. For compact layer, 0.3 g of hydrated ZrO_2 surface passivated ZnO/TiO_2 powder was placed in a vial containing 2 mL deionized water and sonicated until it forms visually translucent solution. To this, a drop of Triton X-200 was added to the vial and sonicated again for 20 min to ensure that the binder was coated onto hydrated nanocomposite particles. Between the spin coatings, the compact layers were slowly heated to 240 °C for gentle curing and kept at this temperature for 10 min and then allowed to naturally cool to room temperature. The slow heat curing step is critical to give the compact layer's structural integrity and further processing stability. This coating procedure was repeated few times to get a desired thickness. At the end, the compact films were sintered at an elevated temperature of 450 °C and kept at this temperature for 30 min and then allowed to cool to room temperature.

2.4. Thick active layer preparation and coating

For thick paste formulation, the pastes were prepared in two steps. First, the mixture of citric acid and ethylene glycol was heated to 70 °C under constant stirring until a visually clear solution was obtained. The paste was prepared with 0.6 g of calcined ZrO_2 surface passivated ZnO/TiO_2 powder using mortar and pestle by adding citric solution in controlled fashion to form continues and smooth colloidal paste with a long shelf life. Finally, the paste was spin-coated on the top of compact layer and this protocol was repeated three times to get a desired thickness or film integrity. The films were sintered in muffle furnace at 450 °C for 30 min and then allowed to cool to room temperature.

2.5. Electrolyte preparation

The supporting electrolyte for DSSC was prepared by mixing 0.03 M iodine (I_2), 0.1 M lithium iodide, 0.5 M 4-*tert*-butylpyridine (tBP) and 0.6 M 1-hexyl-2, 3-dimethyl-imidiazolium iodide (BMII) in a 1:1 volume mixture of acetonitrile and anhydrous ethanol.

2.6. Preparation of platinum electrode

Platinum nanoparticles (Particular GmbH) with particle size ∼70 nm dissolved in acetone (1 g/L) and spray coated on pre-heated FTO glass on hotplate (∼100 °C). The approximate area covered by Pt-layer was about 2.15 cm^2. The spray deposited Pt-electrodes were sintered in a muffle furnace at 450 °C for 30 min in air.

2.7. DSSCs assembly

Sensitization of the photoanode was carried out by immersing the photoanode into a 5.94 mg N719 dye (Solaronix) in 10 mL acetonitrile–ethanol solution for 24 h at room temperature in the dark. Loosely held dye molecules were washed off with ethanol and then dried in air. The dye anchored, and Pt-counter electrodes were assembled into a sealed sandwich-type cell. Effective sealing was achieved by heating the two electrodes with a hot-melt Parafilm® serving as a spacer between the electrodes. The electrolyte solution was injected through pre-drilled channel-holes on the counter electrode and the openings were sealed by a piece of glass. The typical active area of the cell was ∼0.25 cm^2. In the last step, external electrodes were coated with silver paste to establish good electrical contact.

2.8. Characterization methods

2.8.1. SEM/TEM, X-ray diffraction and FT-IR spectra

The morphology of the anode material was characterized using a scanning electron microscope (SEM, Zeiss Supra (40 VP FESEM)) and a transmission electron microscopy (TEM, Hitachi (H7000 FA)) operated at 200 kV. The SEM images were obtained at the voltage of 3 keV with the condenser aperture setting of 20 mm and the sample working distance of 4 mm from the condenser aperture. All the images were acquired with a secondary electron detector. Fourier transform infrared (FTIR) spectrum of the mesoporous composite powder absorption was obtained in the range of 400–4000 cm^{-1} using spectrum 100 of Perkin Elmer spectrophotometer. The anode material calcined at 600 °C was also analyzed in the powder form by X-ray diffraction (XRD) using the Rigaku Ultima IV instrument provided with Ni-filtered CuKα radiation ($\lambda = 1.5406$ Å) at 40 kV and 30 mA. The diffraction angle 2θ was scanned over 20°–80°at a scanning rate of 1° min^{-1} with a step size of 0.025.

For TEM sample preparation, a minute amount of powder composite was dispersed in ethanol and gently high power sonicated to deagglomerate the particles. A drop of stable colloidal suspension was placed on copper grid and allowed to evaporate and dry. Then the grid was inserted for TEM structural imaging and characterization.

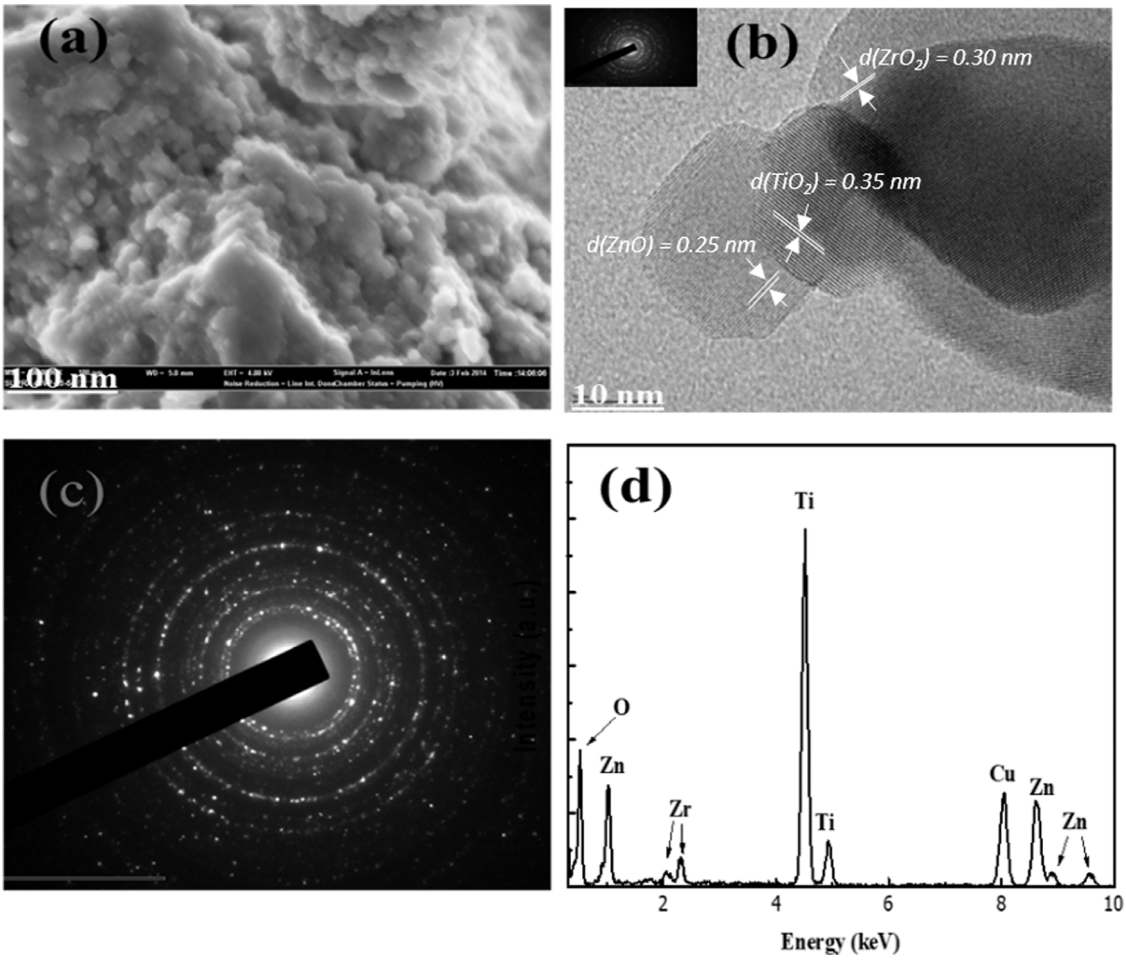

Fig. 1. (a) SEM and (b) TEM images of a nanostructured ZrO_2 surface passivated ZnO/TiO_2compact layer with the corresponding (c) diffraction rings and d) EDX elemental analysis.

2.8.2. Photocurrent density–voltage characteristics (J–V)

J–V curves represent the most basic and direct characterization method to evaluate DSSCs under both illumination and dark conditions. The *J–V* and device quantum efficiency typically are measured under a set of standard testing conditions, such as ambient temperature, input power intensity of 100 mW/cm^2, and simulated sunlight characterized by the spectral power distribution of air mass 1.5 global (AM 1.5G). The light intensity of the xenon light source was adjusted and calibrated by using NREL certified silicon photodiode (S1133-14 for visible to IR range) prior to every measurement. *J–V* characteristics of the devices were measured using an Agilent 4155C Semiconductor Parameter Analyzer over the bias range of 0–1 V, with a step change of 10 mV. Dark currents were measured under the similar conditions, but in darkness. To measure the effectiveness of the cell to convert light, incident photon-to-current efficiency (*IPCE*) spectral response was performed over spectral range of 300–800 nm wavelengths using Newport QE/IPCE system.

2.8.3. Electrochemical impedance spectroscopy (EIS)

Impedance measurements were implemented over the frequency range of 1 Hz to 300 kHz with the modulation signal of 10 mV AC amplitude and near an open-circuit condition. Gamry EChem Analyst is the software used for the fitting of the impedance data to equivalent circuit model. From best closely fitting experimental data, parameters such as charge-transfer resistance at the counter electrode, electron recombination resistance at the film/dye/electrolyte interface, as well as diffusion resistance in the electrolyte can be obtained.

3. Results and discussion

3.1. SEM/TEM

Fig. 1(a) is an SEM image showing the nanostructured compact thin film of a conjoined ZrO_2 surface passivated ZnO/TiO_2 nanoparticles. The SEM images show less conformal porous networking of nanoparticles. The high-resolution HRTEM image (Fig. 1(b)) confirms distinct and inter-necked hierarchal arrangement of a hetero-phase network. The obtained lattice spacing between adjacent fringes in a HRTEM image compared well with the d-spacing value calculated from X-ray diffraction patterns. The lattice spacing is in agreement to well-resolved crystalline planes of TiO_2 and ZnO with the d-spacing of 0.35 nm (i.e. (101) plane of anatase) and 0.25 nm (i.e. (101) wuzurite plane of ZnO), respectively (Fig. 1(b)).

Recently, we reported on a family of non-precious transition metal oxides based photocatalysts for solar water splitting and biomass reforming. Since chemical composition-structure–activity relationships and various physical properties have been discussed in depth, a reader can simply refer to our earlier reported studies (Hussein et al., 2013; Hussein and Shende, 2014). Also, in this work, it is observed that physical properties and structural modifications influence important DSSC performance parameters such as optoelectronic properties, surface sensitivity, dye loading and porosity. Therefore, ZrO_2-modified ZnO/TiO_2 composites have effectively boosted open circuit potential, improved optical and electronic properties such as low band gap and visible light absorption, and high porosity. Among all other factors the enhancement in

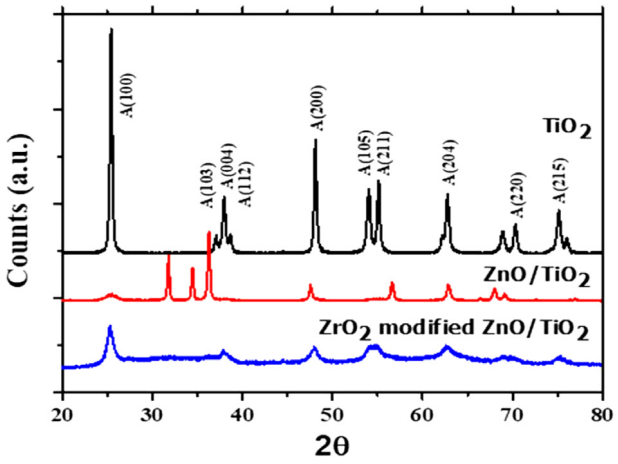

Fig. 2. X-ray diffraction patterns of TiO_2, ZnO/TiO_2 and ZrO_2- surface modified ZnO/TiO_2 powders.

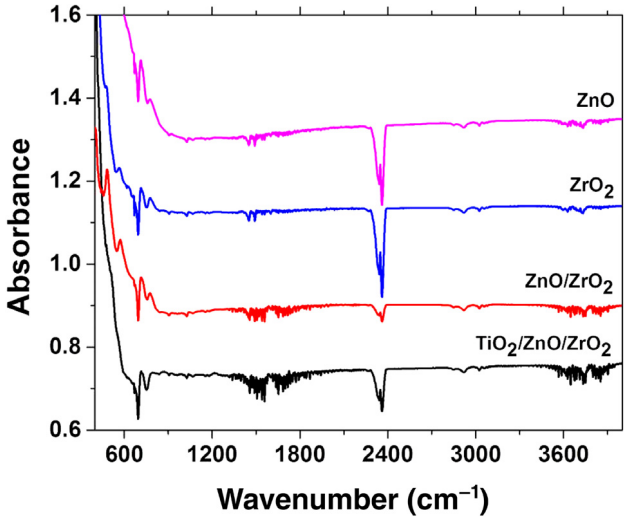

Fig. 3. FTIR spectrum of ZnO, ZrO_2, ZnO/ZrO_2 and ZrO_2 modified TiO_2/ZnO mesoporous powders.

DSSC performance is attributed to better dye loading and multiple light harvesting ability of the photoanode film due to robustness, interconnected porous heterostructure and network.

The hierarchical nanoarchitecture photoanode is usually characterized by high surface area and porosity, and distinct physicochemical surface properties. Such conjoined hierarchical nanostructure provides conductive pathways from the site of electron injection to the charge collecting electrode and allows the redox electrolyte to traverse the nanostructure for efficient electron/hole regeneration. In other words, fast electron transport can be maintained in the device, with the advantage of longer electron life time and high charge mobility that is essential for obtaining higher efficiencies in the cell.

3.2. Powdered X-ray diffraction

Mesoporous ZnO/TiO_2 and ZrO_2 surface modified ZnO/TiO_2 powders obtained after the calcination at 600 °C were analyzed by the X-ray diffraction and the spectra obtained are shown in Fig. 2. A diffraction characteristic belong to anatase TiO_2 is included for visual comparison. Anatase (A) to rutile phase transformation usually begin at about 500 °C. However, presence of transition metals as substitutional ions seems to inhibit anatase to rutile phase transformation even at elevated temperature (600 °C) (Arbiol et al., 2002). Thus, the zinc and/or zirconium ions stabilized TiO_2 only shows anatase phase. Due to secondary phase formation, however, the intensities of those anatase peaks significantly decreased. Upon rutile phase formation, primary diffraction characteristic peaks would appear at around $2\theta = 27.5°$ and 36° (Kyotani et al., 2008); however, no such peaks were observed in the sample.

3.3. FTIR spectrum

FTIR spectrum of the metal oxide powders in the range of 400–6000 cm^{-1} is shown in Fig. 3. Absorption bands around 667, 695 and 753 cm^{-1} could be attributed to Zn–O, Zr–O and Ti–O inter-atomic vibrations (Khan et al., 2015; Ullah et al., 2014). The spectrum exhibits broad absorption peaks in the range of 3500–3800 cm^{-1} corresponding to the stretching mode of the O–H hydroxyl group of the water adsorbed on the surface of nanoparticles. All oxide powders and its composite exhibit absorption bands in the range of 2340–2360 cm^{-1}, representing O–H stretching vibrational modes associated with O–Zn–O, O–Zr–O and O–Ti–O (Pandey et al., 2015). With respect pristine ZnO and ZrO_2 phases, both ZnO/TiO_2 and ZrO_2 modified ZnO/TiO_2 nanocomposites retained the prominent peaks positions at ∼2360 cm^{-1} but with slight decrease in peaks intensity, thus confirming secondary phase formation (Hussein and Shende, 2014).

3.4. DSSC performance

Hierarchically nanostructured photoanode of ZrO_2 surface passivated ZnO/TiO_2 hetero-phase were adapted in the DSSC sandwich configuration. The inter-necked hetero-phase containing different nanocrystalline metal oxide aggregates and particle size distributions have improved connectivity amongst nanoparticles and porosity, quality of thin film coating and adherence on a FTO substrate, thus, facilitating high dye loading (i.e. light harvesting), efficient and continuous charge carrier transport at the FTO/photoanode interface, consequently contributed to better solar-to-electricity conversion efficiency and performance. The cell assembly was evaluated both in the dark and under simulated AM 1.5 solar light conditions. Fig. 4 depicts illuminated and dark current *J–V* characteristics of ZnO/TiO_2 as a reference and ZrO_2 surface passivated ZnO/TiO_2 photoanodes. The two cells were identically prepared and assembled. The characteristic photovoltaic parameters of interest such as open-circuit voltage (V_{oc}), short circuit photocurrent density (J_{sc}), fill factor (FF) and power conversion efficiency (η) obtained from Fig. 4(a) are tabulated in Table 1. It also displays literature values of the similar studies (i.e. metal oxide photoanodes, '1 sun' illumination, electrolyte and N719 dye) and compares power conversion efficiencies and other DSSC performance parameters with our layered ZrO_2-modified ZnO/TiO_2 photoanodes.

For comparison, the reference cell assembled with ZnO/TiO_2 photoelectrode exhibited a short-circuit current density (J_{sc}) of 8.9 mA/cm^2, an open circuit voltage (V_{oc}) of 0.75 V, a fill factor (FF) of 50% and an overall conversion efficiency (η) of 3.41%. Referring to Fig. 4(a), the cell prepared with the ZrO_2 surface modified ZnO/TiO_2 compact layer exhibited improved J_{sc} and V_{oc} by 35% and 13%, respectively. The corresponding solar light-to-electricity conversion efficiency of new hetero-phase structures, $\eta = \sim 6.97\%$ with FF = 0.6 were obtained. These measurements were performed under '1 sun' illumination; however, few measurements were also carried out at other illumination intensities (data not included).

The V_{oc} of the DSSCs prepared with ZrO_2 surface passivated ZnO/TiO_2 photoanode is about 130 mV higher compared to that

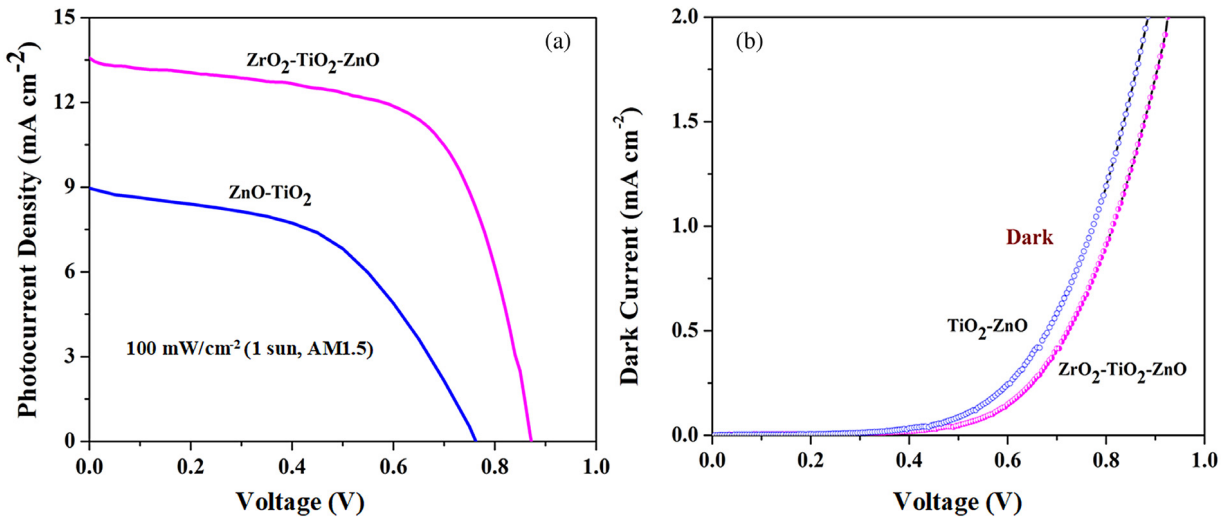

Fig. 4. Photocurrent–voltage characteristics measured under simulated AM 1.5 solar light illumination (a), and its corresponding dark J–V characteristics (b).

Table 1
J–V parameters of the DSSCs prepared with un-passivated ZnO/TiO_2 and ZrO_2 surface passivated ZnO/TiO_2 photoanodes under simulated solar light illumination.

Photoanode	Voc (V)	Jsc (mA cm^{-2})	FF	η (%)	Ref
TiO_2 (NPs)[a]	0.75	10.0	0.65	4.90	(Henning et al., 2013)
TiO_2 (NPs)	0.82	9.32	0.72	5.45	(Chung et al., 2012)
TiO_2 (NTs)[a]	0.72	7.16	0.70	3.63	(Chung et al., 2012)
TiO_2 (NRs)[a]	0.80	13.6	0.51	5.80	(Liao et al., 2012)
TiO_2 (NWs)[a]	0.79	7.91	0.69	4.32	(Fujihara et al., 2007)
ZrO_2/TiO_2	0.59	12.5	0.72	5.10	(Kitiyanan et al., 2005)
ZnO/TiO_2	0.74	8.96	0.50	3.41	This work
$ZrO_2/ZnO/TiO_2$	0.87	13.6	0.65	6.97	This work

[a] Nanoparticles (NPs), Nanotubes (NTs), Nanorods (NRs) and Nanowires (NWs).

of reference cell of ZnO/TiO_2 photoelectrode. Since all the other components of the cells such as electrolyte, dye, counter electrode and method of preparation is the same, the differences in performance is mainly due to photoelectrode properties. The high V_{oc} is attributed to the negative shift of the conduction band edge and flat band potentials (Gu et al., 2014) with respect to the redox potential of the electrolyte (Tian et al., 2013). The EIS measurement subjected to different bias potentials confirms an apparent shift in the Fermi energy level toward more negative. The negative shift arising from ZrO_2 incorporation in the ZnO/TiO_2 hybrid was reported in our previous work (Hussein and Shende, 2014) and was responsible for bandgap narrowing. It is anticipated that the highly positioned ZrO_2 conduction band edge on the energy scale creates potential barrier for electron transport at an FTO/photoanode interface. Thus, the surface passivation reduces the charge recombination rate, thus increasing the V_{oc} of the device. The enhancement in V_{oc} further interpreted as a reduced in the back electron transfer to the triiodide species in the electrolyte (Huang et al., 1997) and at Pt-electrode/electrolyte interface. The effect of reduced charge recombination is supported by smaller charge transfer resistance obtained (Table 2) from EIS result at the counter electrode interface.

On the other hand, enhancement in current density is attributed to monolayer dye adsorption as the surfaces and dye loading capacity are strongly influenced by the electrostatic and interfacial chemical interactions (Annamalai et al., 2011; Bai et al., 2014). The amount of dye adsorption on the photoelectrode affects the photocurrent. Therefore, the interface charge state between hetero-phase metal oxides and dye molecules is particularly of interest as it determines dye loading capacity, thus the electron injection efficiency (Annamalai et al., 2011; Akimov et al., 2013; Thavasi et al., 2009). Surfaces with higher isoelectric points are preferable for the attachment of dye molecules. For a hetero-phase derived photoelectrode, which exhibits the highest isoelectric point (9.7) and hierarchical positively charged surfaces, preferably accommodates more negatively charged dye molecules as possible (Annamalai et al., 2011; Thavasi et al., 2009; Thapa et al., 2014). The specificity and surface charges in hetero-phase metal oxides enhances the electronic affinity of the sensitizers (i.e. carboxylate groups) to effectively anchor onto the support structures. Thus, the enhancement in the J_{sc} was anticipated with compact metal oxide layers of large bandgap energy and high isoelectric points. To further clarify the quality of the photoanode in DSSC operation, EIS spectra were analyzed using the software EChem Analyst as discussed later. Improved overall device performance was validated and ascribed to the superior electron transport and longer electron lifetime as elucidated by impedance spectroscopy. In line with the improved photovoltaic performance, the semi-transparent ZrO_2 surface passivated ZnO/TiO_2 photoanode film exhibited high transparency (~70%) in the 500–600 nm range.

3.5. EIS and equivalent circuit fitting results

To gain insight into the interfacial electronic as well as ionic charge transport processes, the devices were analyzed by electrochemical impedance spectroscopy. Fig. 5(a) shows the Nyquist plot of the DSSCs configuration and impedance spectra obtained for ZrO_2 passivated ZnO/TiO_2 photoanode. Here, the Nyquist plot displays the impedance behavior of an interfacial electrochemical response among cell elements in an equivalent circuit. The impedance spectra show three distinct semicircles in a complex plane situated in high, intermediate, and low frequency regimes.

Table 2
The impedance parameters obtained by fitting the experimental data to the proposed equivalent circuit of the reference cell based on ZnO/TiO_2 and a ZrO_2 surface passivated ZnO/TiO_2 photoanodes as a function of applied bias.

Applied bias (V)	R_{ohm} (Ω cm^2)	C_1 (uFS^{a-1})	R_1 (Ω cm^2)	C_2 (uFS^{a-1})	R_2 (Ω cm^2)
0.5[a]	11.64	33.0	1.8	57.6	95.6
0.5	11.63	25.1	1.6	63.4	48.5
0.6	11.65	19.5	1.4	70.2	29.2
0.7	11.63	20.3	1.3	80.9	18.5

[a] ZnO/TiO_2 based DSSCs.

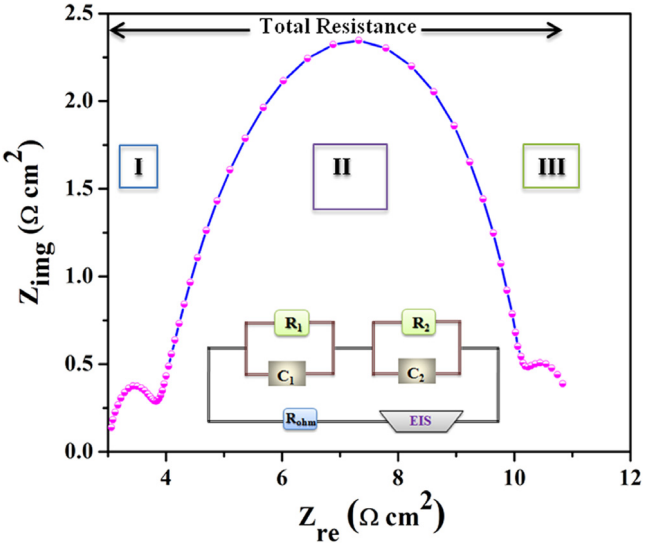

Fig. 5. The impedance spectra obtained for optimized compact layers and fitted using the equivalent circuit model (inset).

The high frequency semicircle (I) is ascribed to the charge transfer resistance at the electrolyte/platinum counter electrode. The semicircles (II and III) at the intermediate and low frequency range correspond to charge transfer resistances at the photoanode/dye/electrolyte interface and the Nernst diffusion of the redox couple within the electrolyte (Sarker et al., 2014), respectively. Nyquist plots fitted to the equivalent circuit represented in Fig. 5 (inset). As illustrated, the overall equivalent circuit model composed of two R–C loops with electrochemical parameters R_1, C_1, and R_2, C_2, is in series with the ohmic resistance, R_{ohm}. The electron charge transfer at electrolyte/platinum counter electrode and photoanode/dye/electrolyte interfaces are represented by R_1 and R_2, respectively. Thus, the EIS data were analyzed by fitting to an equivalent electrical circuit model. Iteratively estimated components of the two electrodes and ohmic contribution is given in Table 2. The resistances obtained were normalized to the geometric active surface area. The total resistance is sum of all the contributions given as $R_{total} = R_{ohm} + R_1 + R_2$. The overall goal is to minimize the total resistance in the cell.

Referring to Fig. 4(b) above, the higher onset potential in the dark and larger V_{oc} under illumination further confirms the ZrO_2surface passivated ZnO/TiO_2 compact layer effectively retards back electron transfer or direct physical contact between FTO and electrolyte. Particularly, the reduction in the dark current further suggests that the electron back transfer from photoelectrode to the redox ions in the electrolyte ($2e^- + I_3^- \rightarrow 3I^-$) was minimized. For ZrO_2 surface passivated ZnO/TiO_2 compact layer, the onset potential in the dark occurred at ~0.61 V, nearly over 0.1 V larger than that of un-passivated ZnO/TiO_2 layer shown in Fig. 4(b).

Fig. 6 and Table 2 together illustrates the variations of the impedance spectral parameters related to interfacial electronic processes obtained as the function of applied forward bias of 0.5–0.7 V. As we previously eluded to, the impedance response obtained in the high and low frequency domains correspond to charge transfer through electrolyte/counter electrode and I3- diffusion in the electrolyte, respectively. The arcs show similar electrochemical properties and did not differ so much with bias potential. However, the arcs situated at the intermediate frequency range strongly depend on the applied bias potential and correspond to the impedance of charge transfer the photoanode/dye/electrolyte interface. The interpretation of the spectral change with the applied forward bias supports the bias dependence of electron injection into the conduction band.

As seen in Table 2, there is a decrease in interfacial charge transfer resistance (R_2) and an increase in a chemical capacitance (C_2) upon increasing the bias potentials. On the other hand, no significant changes in R_{ohm} or R_1 values can be seen with applied bias potentials or between ZnO/TiO_2 and ZrO_2 modified ZnO/TiO_2 photoanodes. However, at the same 0.5 V applied bias voltage, the charge transport resistance R_2 is 48.5 Ω cm^2 for ZrO_2 surface modified compact layer verses 95.6 Ω cm^2 for ZnO/TiO_2 alone. This observation provides direct evidence for a much lower charge transfer resistance, which could be a crucial factor for the improvement of the performance of the DSSCs by employing interpenetrated architectures. It is also implying that DSSCs made of ZrO_2 surface passivated ZnO/TiO_2 compact photoanode layer is effective in minimizing charge recombination rate and favors charge collection by FTO substrate than that of ZnO/TiO_2 photoanode alone. It further highlights the significance of ZrO_2 surface passivation in improving capacitance at the electrode/dye/electrolyte interface and electron life time, thus favoring charge collection in the external circuit.

3.6. Effect of compact layer thickness on J–V characteristics

Photocurrent–voltage response was evaluated to establish effects of film layer thickness on the device performance. Fig. 7(a) and (b) shows the relationship between the J_{sc} and the compact layer film thickness and the corresponding photocurrent action spectrum of the device prepared of multiple deposition cycles. As observed from the current–voltage characteristic, the cell performance is strongly affected by the thickness of the compact layers as directly controls the photon adsorption. Clearly, the current density greatly enhanced with more compact layers coating. However, as Fig. 7(a) further illustrates, the V_{oc} or FF was hardly affected by the film thickness. A similar observation was reported in the studies by Wang et al. (2012c). The FF and V_{oc} were in the range of 0.62–0.65 V and 0.85–0.87 V, respectively, for the devices prepared with different compact layer thicknesses. It should be noted that, normally the light harvesting in a thin layer is lower than that of thicker layer due to less dye uptake and the absorption depth. However, the path and resistances to the photo-generated electrons through the photoanode grows simultaneously with the film thickness (Fabregat-Santiago et al., 2008; Chen et al., 2010). Therefore, keeping the optimum thickness is critical to maintain sufficient optical absorption as well as efficient charge transport across the nanostructured photoanode film.

Fig. 7(b) depicts the incident photocurrent conversion efficiency (IPCE) spectrum of the DSSC prepared with multiple passivation layers as the function of wavelength. The photoanode have electronic absorption spectra in the visible region (400–700 nm) and closely resembles N719 dye (Cheema et al., 2014). This is attributed to enhanced N719 dye loading due to high porosity of the composite photoanode. IPCE values higher than 60% were observed in the 400–600 nm spectral range. The maximum IPCE observed is ~70% at 575 nm suggesting strong photon harvesting characteristics, high photon-to-current conversion and performance.

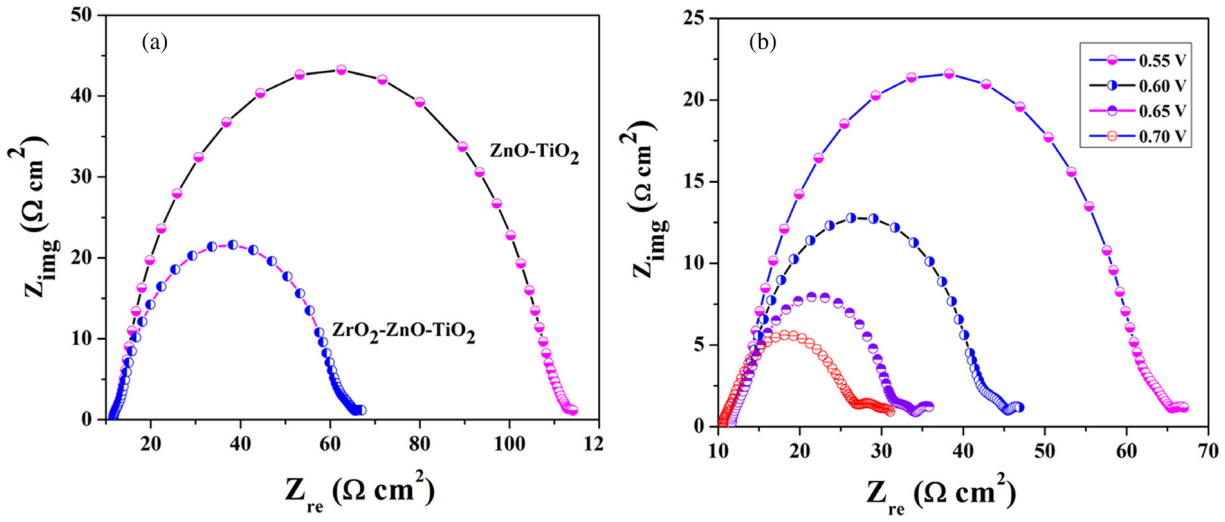

Fig. 6. Impedance spectra obtained for (a) un-passivated ZnO/TiO_2 and ZrO_2 surface passivated ZnO/TiO_2 based solar cells and (b) the changes in interfacial electronic processes of the ZrO_2 surface passivated ZnO/TiO_2 as function of applied forward bias from 0.55 to 0.7 V.

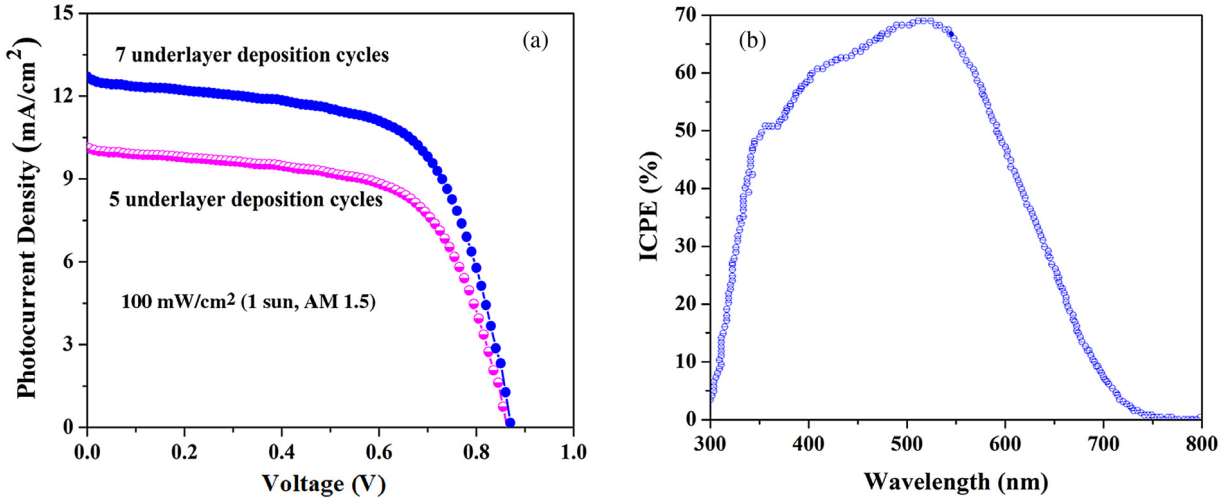

Fig. 7. (a) Photocurrent–voltage characteristics of the ZrO_2 surface passivated ZnO/TiO_2 compact layer at varying coating thickness, and (b) the corresponding photocurrent action spectrum of the device prepared with multiple deposition cycles.

4. Conclusions

The interpenetrating networks arising from hetero-phase contact at the nanoscale in the ZrO_2 surface passivated ZnO/TiO_2 system were shown to affect the performance of the cell on multiple levels. Mainly, the mesoscopic hetero-phase network enhances photon capture by exerting a dual function to scatter light and photo-generate charge carriers. The dye loading ability and reduced charge recombination losses, yielding higher open circuit potential, photocurrent and moderately higher fill factor that govern the efficiency of the cell. The DSSC with optimized compact layer of ZrO_2 surface passivated ZnO/TiO_2 hetero-phase network produced a relatively high V_{oc} of 0.87 V, J_{sc} of 13.6 mA cm^{-2} and FF of 0.65, which gives an overall light-to-electricity conversion efficiency of ∼6.97%. The larger turn-on voltage in the dark and larger V_{oc} in the illuminated J–V characteristics implies that the ZrO_2 surface passivation effectively retarded the interfacial charge recombination rate, consequently leading to improved electron injection and transport. The observed increase in J_{sc} could be attributed to the increased electron lifetime in conjoined ZrO_2 surface passivated ZnO/TiO_2 compact film, thus providing improved electron percolation pathways as compared with the reference photoelectrode solar cells. In addition, the reduction in R_2 further supports a decrease in the charge recombination rate with redox species in the electrolyte or the oxidizing dye, thus resulting in fast charge transfer processes and enhancement in the DSSCs performance.

Acknowledgments

The authors acknowledge the financial and research assistantship support from NSF DGE-0903685 and NSF EPS-0903804.

References

Akimov, A.V., Neukirch, A.J., Prezhdo, O.V., 2013. Chem. Rev. 113, 4496–4565.
Annamalai, A., Eo, Y.D., Im, C., Lee, M.-J., 2011. Mater. Charact. 62, 1007–1015.
Arbiol, J.C.J., Dezanneau, G., Cirera, A., Peiró, F., Cornet, A., Morante, J.R., 2002. J. Appl. Phys. 92.
Bai, Y., Mora-Seró, I.n., De Angelis, F., Bisquert, J., Wang, P., 2014. Chem. Rev. 114, 10095–10130.
Cheema, H., Islam, A., Han, L., Gautam, B., Younts, R., Gundogdu, K., El-Shafei, A., 2014. J. Mater. Chem. A 2, 14228–14235.
Chen, P., Brillet, J., Bala, H., Wang, P., Zakeeruddin, S.M., Grätzel, M., 2009. J. Mater. Chem. 19, 5325–5328.
Chen, L.-C., Tsai, S.-F., Chen, J.-H., Wang, G.-W., 2013. Int. J. Photoenergy 2013, 9.

Chen, L.-M., Xu, Z., Hong, Z., Yang, Y., 2010. J. Mater. Chem. 20, 2575–2598.
Chung, K.-H., Rahman, M.M., Son, H.-S., Lee, J.-J., 2012. Int. J. Photoenergy 2012, 1–6.
Docampo, P., Guldin, S., Leijtens, T., Noel, N.K., Steiner, U., Snaith, H.J., 2014. Adv. Mater. 26, 4013–4030.
Duan, Y., Zheng, J., Fu, N., Fang, Y., Liu, T., Zhang, Q., Zhou, X., Lin, Y., Pan, F., 2015. J. Mater. Chem. A 3, 3066–3073.
Fabregat-Santiago, F., Bisquert, J., Cevey, L., Chen, P., Wang, M., Zakeeruddin, S.M., Grätzel, M., 2008. J. Am. Chem. Soc. 131, 558–562.
Fujihara, K., Kumar, A., Jose, R., Ramakrishna, S., Uchida, S., 2007. Nanotechnology 18, 365709.
Gao, Y., Zhu, J., An, H., Yan, P., Huang, B., Chen, R., Fan, F., Li, C., 2017. J. Phys. Chem. Lett. 8, 1419–1423.
Grätzel, M., 2001. Nature 414, 338–344.
Grätzel, M., 2005. Inorg. Chem. 44, 6841–6851.
Green, M.A., Emery, K., Hishikawa, Y., Warta, W., Dunlop, E.D., 2011. Prog. Photovolt., Res. Appl. 19, 565–572.
Gregg, B.A., Pichot, F., Ferrere, S., Fields, C.L., 2001. J. Phys. Chem. B 05, 1422–1429.
Gu, F., Huang, W., Wang, S., Cheng, X., Hu, Y., Lee, P.S., 2014. Phys. Chem. Chem. Phys. 16, 25679–25683.
Gu, C., Jia, C., Guo, X., 2017. Mater. Chem. Front. 1, 2125–2131.
Henning, A., Günzburger, G., Jöhr, R., Rosenwaks, Y., Bozic-Weber, B., Housecroft, C.E., Constable, E.C., Meyer, E., Glatzel, T., 2013. Beilstein J. Nanotechnol. 4, 418–428.
Hod, I., Shalom, M., Tachan, Z., Rühle, S., Zaban, A., 2010. J. Phys. Chem. C 114, 10015–10018.
Huang, S.Y., Schlichthörl, G., Nozik, A.J., Grätzel, M., Frank, A.J., 1997. J. Phys. Chem. B 101, 2576–2582.
Hussein, A.M., Mahoney, L., Peng, R., Kibombo, H., Wu, C.-M., Koodali, R.T., Shende, R., 2013. J. Renew. Sustain. Energy 5, 033118.
Hussein, A.M., Shende, R.V., 2014. Int. J. Hydrogen Energy 39, 5557–5568.
Jose, R., Thavasi, V., Ramakrishna, S., 2009. J. Am. Ceram. Soc. 92, 289–301.
Katz, M.J., Vermeer, M.J., Farha, O.K., Pellin, M.J., Hupp, J.T., 2012. Langmuir 29, 806–814.
Khan, M., Naqvi, A.H., Ahmad, M., 2015. Toxicol. Rep. 2, 765–774.
Kitiyanan, A., Ngamsinlapasathian, S., Pavasupree, S., Yoshikawa, S., 2005. J. Solid State Chem. 178, 1044–1048.
Kyotani, M., Goto, H., Suda, K., Nagai, T., Matsui, Y., Akagi, K., 2008. J. Nanosci. Nanotechnol. 8, 1999–2004.
Law, M., Greene, L.E., Radenovic, A., Kuykendall, T., Liphardt, J., Yang, P., 2006. J. Phys. Chem. B 110, 22652–22663.
Lee, S., Han, G.S., Lee, J.-H., Lee, J.-K., Jung, H.S., 2012. Electrochim. Acta 74, 83–86.
Liao, J.-Y., Lei, B.-X., Chen, H.-Y., Kuang, D.-B., Su, C.-Y., 2012. Energy Environ. Sci. 5, 5750–5757.
Liu, R., Yang, Qiang, Wein-Duo, Liu, Liang-Sheng, Hsin-Yi, 2012. J. Power Sources 220, 153–159.
Mathew, S., Yella, A., Gao, P., Humphry-Baker, R., Curchod, B.F., Ashari-Astani, N., Tavernelli, I., Rothlisberger, U., Nazeeruddin, M.K., Gratzel, M., 2014. Nat. Chem. 6, 242–247.
Milan, R., Selopal, G.S., Epifani, M., Natile, M.M., Sberveglieri, G., Vomiero, A., Concina, I., 2015. Sci. Rep. 5, 14523.
Mohan, V.M., Shimomura, M., Murakami, K., 2012. J. Nanosci. Nanotechnol. 12, 433–438.
Ofir, A., Grinis, L., Zaban, A., 2008. J. Phys. Chem. C 112, 2779–2783.
Pai, K.R.N., Anjusree, G.S., Deepak, T.G., Subash, D., Nair, S.V., Nair, A.S., 2014. RSC Adv. 4, 36821–36827.
Palomares, E., Clifford, J.N., Haque, S.A., Lutz, T., Durrant, J.R., 2003. J. Am. Chem. Soc. 125, 475–482.
Pandey, S.M.R.K., Karmakar, Avik, Sharma, M.P., Bajpai, P.K., 2015. J. Pure Appl. Ind. Phys. 5.
Sarker, S., Ahammad, A.J.S., Seo, H.W., Kim, D.M., 2014. Int. J. Photoenergy 2014, 17.
Shang, X., Guo, Z., Gan, W., Zhou, R., Ma, C., Hu, K., Niu, H., Xu, J., 2015. Ionics 22, 435–443.
Shintaro Ueno, N.H.a., Fujihara, S., 2011. Int. J. Nanoparticles 4.
Smiglak, M., Pringle, J., Lu, X., Han, L., Zhang, S., Gao, H., MacFarlane, D., Rogers, R., 2014. Chem. Commun. 50, 9228–9250.
Somasundaran, P., Chin, M., Latosiewicz, U.T., Tuller, H.L., Barbiellini, B., Renugopalakrishnan, V., Reisner, D., 2011. Bionanotechnology II: Global Prospects. CRC Press, Boca Raton, FL.
Tang, X., Wang, Y., Cao, G., 2013. J. Electrochem. Soc. 694, 6–11.
Thapa, A., Zai, J., Elbohy, H., Poudel, P., Adhikari, N., Qian, X., Qiao, Q., 2014. Nano Res. 7, 1154–1163.
Thavasi, V., Renugopalakrishnan, V., Jose, R., Ramakrishna, S., 2009. Mater. Sci. Eng. R 63, 81–99.
Tian, J., Zhang, Q., Zhang, L., Gao, R., Shen, L., Zhang, S., Qu, X., Cao, G., 2013. Nanoscale 5, 936–943.
Toivola, M., Halme, J., Miettunen, K., Aitola, K., Lund, P.D., 2009. Int. J. Energy Res. 33, 1145–1160.
Ullah, H., Khan, K.A., Khan, W.U., 2014. Chin. J. Chem. Phys. 27, 548–554.
Veerappan, G., Jung, D.-W., Kwon, J., Choi, J.M., Heo, N., Yi, G.-R., Park, J.H., 2014. Langmuir 30, 3010–3018.
Wang, M., Bai, J., Le Formal, F., Moon, S.-J., Cevey-Ha, L., Humphry-Baker, R., Grätzel, C., Zakeeruddin, S.M., Grätzel, M., 2012a. J. Phys. Chem. C 116, 3266–3273.
Wang, J., Jin, E.M., Park, J.Y., Wang, W.L., Zhao, X.G., Gu, H.B., 2012b. Nanoscale Res. Lett. 7, 98.
Wang, Y., Wu, M., Lin, X., Hagfeldt, A., Ma, T., 2012c. Eur. J. Inorg. Chem. 2012, 3557–3561.
Yella, A., Lee, H.-W., Tsao, H.N., Yi, C., Chandiran, A.K., Nazeeruddin, M.K., Diau, E.W.-G., Yeh, C.-Y., Zakeeruddin, S.M., Grätzel, M., 2011. Science 334, 629–634.
Yong, S.-M., Nikolay, T., Ahn, B.T., Kim, D.K., 2013. J. Alloys Compd. 547, 113–117.
Yu, H., Zhang, S., Zhao, H., Will, G., Liu, P., 2009. Electrochim. Acta 54, 1319–1324.